prosthesis

MDPI

Article

Design of a Compliant Sternum Prosthesis for Improving Respiratory Dynamics

Octavio Ramírez [1], Christopher René Torres-SanMiguel [1,*] and Marco Ceccarelli [2]

[1] Instituto Politécnico Nacional, Escuela Superior de Ingeniería Mecánica y Eléctrica, Sección de Estudios de Posgrado e Investigación, Unidad Zacatenco, Mexico City 07738, Mexico
[2] Laboratory of Robot Mechatronics LARM2, Department of Industrial Engineering, University of Rome Tor Vergata, 00133 Rome, Italy; marco.ceccarelli@uniroma2.it
* Correspondence: ctorress@ipn.mx

Abstract: This study presents a novel approach to sternum prosthesis design, aiming to address the limitations of the current solutions by employing compliant mechanisms. The research focuses on developing a prosthetic design capable of generating lifting movements on ribs during breathing. First, a videogrammetry experimental test and virtual simulations were conducted to ascertain the vertical forces applied to each sternum joint. Subsequently, a compliant mechanism design was initiated, involving optimization and finite element analysis (FEM). A comprehensive kinematic performance analysis was performed to evaluate the prosthetic design. The results indicate that the obtained displacements of each rib closely align with those reported in the existing literature, demonstrating the effectiveness of the proposed solution. In conclusion, the developed sternum prosthesis exhibits the capability to recover approximately 56% of the ribs' natural movements, highlighting its potential as an innovative and promising solution in the field of chest prosthetics.

Keywords: compliant mechanism; sternum prosthesis; respiratory dynamics; rib movement

Citation: Ramírez, O.; Torres-SanMiguel, C.R.; Ceccarelli, M. Design of a Compliant Sternum Prosthesis for Improving Respiratory Dynamics. *Prosthesis* **2024**, *6*, 561–581. https://doi.org/10.3390/prosthesis6030040

Academic Editors: Marco Cicciu and Gabriele Cervino

Received: 19 February 2024
Revised: 3 May 2024
Accepted: 14 May 2024
Published: 28 May 2024

1. Introduction

In the realm of medical advancements, the field of prosthetics continually seeks innovative solutions to enhance the quality of life for individuals facing unique challenges. This study delves into the development of a pioneering sternum prosthesis, leveraging compliant mechanisms to introduce lifting movements on ribs during breathing. The sternum plays a crucial role in chest stability, and disruptions due to surgical interventions or traumatic injuries necessitate effective prosthetic interventions. The current prosthetic designs often fall short of replicating the intricate dynamics of natural chest movements, prompting the exploration of novel approaches. Previous sternum prosthetics, designed to address the need for chest stability post-surgery or trauma, often struggle to replicate the nuanced biomechanics of the natural sternum. Rigid prostheses, though structurally supportive, can be limited in accommodating dynamic chest movements during breathing. These challenges highlight the ongoing pursuit of more sophisticated solutions.

Sternum reconstruction becomes necessary in instances of wound infections, trauma, or tumors [1]. Sternal wound infection, albeit infrequent, poses a complication post-chest surgery, with an incidence ranging from 0.5% to 6% of patients [2]. Thoracic bone tumors are rare, affecting less than 2% of the population [3]. In both scenarios, the replacement of a damaged sternum area using a prosthesis is a viable option [4].

A diverse array of devices has emerged for treating sternal lesions. The inaugural report dates back to 1961, featuring a device crafted by Sillar [5], which outlines a clinical case involving a stainless steel plate designed to address fractures in the patient's sternum. Notably, this device stands out as the first to be meticulously shaped to morphologically conform to the sternum's surface, with design precision guided by radiographs as reference instruments. In 1971, Alonso [6] introduced a sternum replacement device designed for

cases where the sternum needed removal due to a malignant tumor. This device consisted of an acrylic resin plate, surgically sutured to both the clavicles and ribs. In 2015, [7] devised a partial sternal endoprosthesis in response to a cancerous tumor. A notable feature of this innovation is its design, which incorporates a fixation system for the ribs. The reconstruction process involved the utilization of computed tomography. Significantly, this endoprosthesis marked a groundbreaking achievement as the first to be manufactured using 3D printing with titanium. In 2017, Cano [8] introduced a titanium-based total sternal endoprosthesis that replicated the sternum, incorporating bilaterally articulated ribs. A notable innovation in this design is the inclusion of a flexible system, enabling the ribs to flex and lengthen during respiratory movements, although the extent of the recovered movements is not specified. In 2019, Wang [9] documented two clinical cases involving the development of a partial sternum endoprosthesis model. This design stands out for its unique manufacturing process, utilizing carbon fiber through 3D printing. As highlighted by the author, the microporous structure of the material is emphasized for its facilitation of tissue ingrowth.

The use of compliant mechanisms in prosthetic design is currently limited. Despite their potential benefits, these flexible structures remain underutilized in the broader context of prosthetics. Below are some instances of its application. In a study by Halverson [10], a compliant mechanism analysis approach was used to develop a pseudo-rigid body model (PRBM) for the lower lumbar spine. The PRBM successfully predicted the moment–rotation response and relative movement patterns of the sample, aligning well with in vitro test results. In [11], a spinal implant was designed to stabilize the spine amidst rigidity loss due to injury, degeneration, or surgery. The device, featuring a laminar emergent torsional joint (LET) divided into two parts and anchored to the vertebral pedicles, significantly enhanced the mechanical stability of the spinal segment, as indicated by the author's experimental results. Hong [12] proposed a compliant mechanism implant for the proximal interphalangeal joint, enabling flexion and extension in the sagittal plane. The design features circular joint surfaces connected by three flexible straps, ensuring the correct movement and alignment of the adjacent phalanges.

The purpose of this work is to present a comprehensive investigation into the feasibility and effectiveness of a compliant mechanism-based sternum prosthesis. By employing a multidisciplinary approach encompassing videogrammetry experimental tests, virtual simulations, optimization, finite element analysis, and kinematic performance evaluations, this research aims to bridge existing gaps in sternum prosthetics. The significance of this study lies in its potential to provide a transformative solution for individuals with compromised sternal integrity, offering not only stability but also the restoration of natural rib movements during respiration. As an innovative stride in the realm of chest prosthetics, the outcomes of this research hold promise in significantly improving the overall functionality and comfort of sternum prostheses, thereby enhancing the rehabilitation and well-being of those in need.

2. Materials and Methods

Designing a sternum prosthesis is an intricate and personalized process. A standardized model is not feasible due to various factors like the patient's age, anthropometric measurements of the rib cage, the extent of the missing bone elements, and the presence of degenerative diseases like osteoporosis [13]. Figure 1 illustrates the methodology employed for sternum endoprosthesis design.

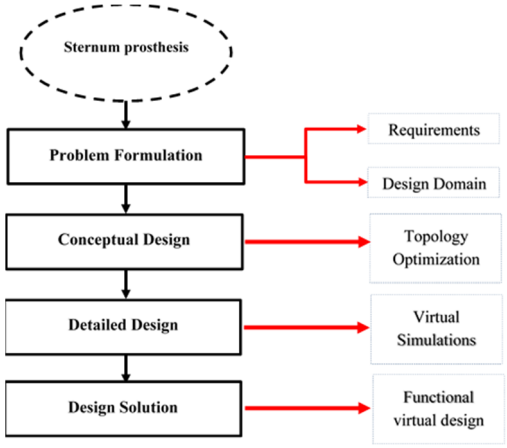

Figure 1. Methodology for a sternum endoprosthesis design adapted from [14].

2.1. Problem Formulation

The primary aim of this study was to develop a sternum prosthesis equipped with a compliant mechanism to enhance respiratory dynamics. The current research endeavors are directed toward three critical categories of requirements: clinical, biomechanical, and pertinent features. In accordance with clinical requisites, the endoprosthesis design must facilitate swift surgical procedures to minimize patient complications. Additionally, the endoprosthesis should possess multifunctionality, enabling its utilization for both partial sternum replacement and sternal closure during open-heart surgeries. The delineated requirements essential for designing a sternum endoprosthesis are summarized in Figure 2.

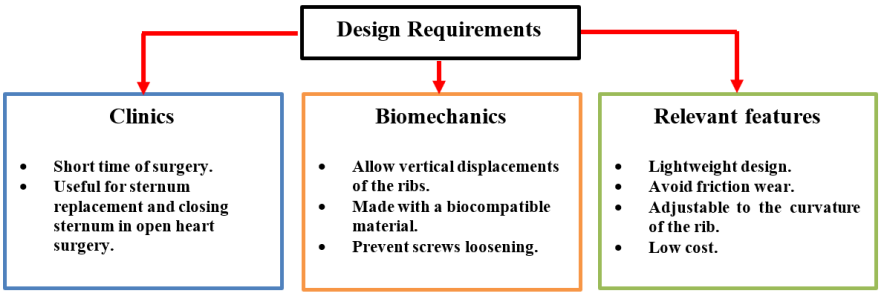

Figure 2. Design requirements for a sternum prosthesis design.

Design Domain

During respiration, the thoracic cavity expands owing to the contraction of the inspiratory muscles. These contractions lead to an augmentation in thoracic volume [15]. As a consequence of rib elevation, two distinct movements manifest within the thoracic cage, one of which is termed the "bucket-handle movement". This motion contributes to the enlargement of the transverse diameter of the thorax [16]. The "pump-handle movement" involves the elevation of the ribs, consequently augmenting the anteroposterior diameter of the thorax [17]. This action results in the upward and downward motion of the sternum, as depicted in Figure 3.

The vertical movement of the joint between the rib and the sternum was analyzed as it constitutes the region of the sternum where elevation occurs during each breath, facilitating the raising of individual ribs.

The design domain area pertains to the available space for developing the compliant mechanism. A two-dimensional domain with symmetry concerning the y-axis was adopted to streamline the solution computation time. The boundary conditions were set with one end of the structure fixed as a beam while an upward vertical load was applied at the free end. This load represented the force exerted by the intercostal muscles to elevate the rib during each exhalation. The design domain area is illustrated in Figure 4.

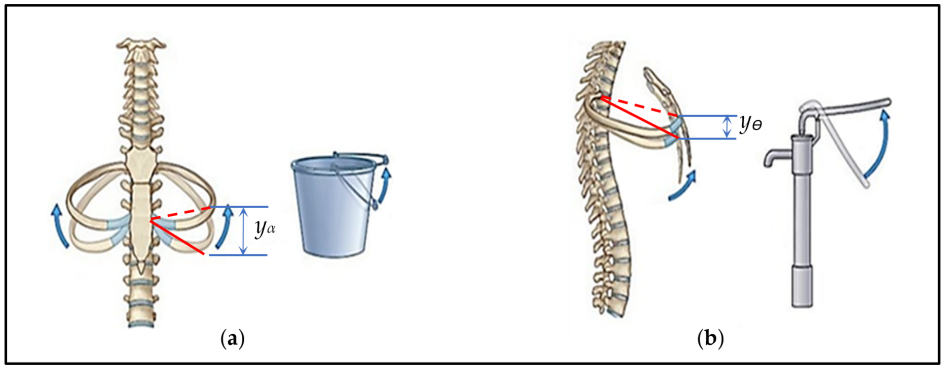

Figure 3. Characteristic movements of the thorax during breathing: (**a**) vertical displacement of bucket-handle movement; (**b**) vertical displacement of pump-handle movement.

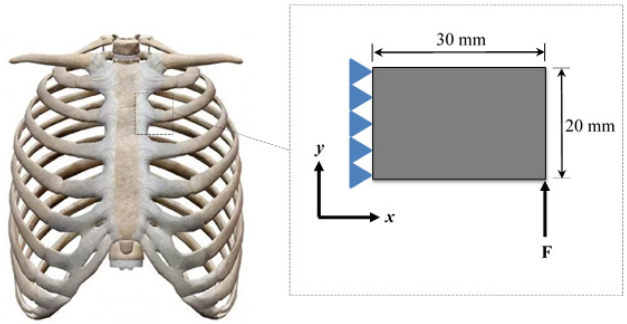

Figure 4. Design domain and boundary conditions for a sternum rib joint.

2.2. Conceptual Design Using the Topology Optimization Method (TOM)

Topological optimization is a mathematical analysis method focused on optimizing material distribution within a defined design space while considering designated loads. The objective is to create a model capable of performing desired functions effectively, as outlined by [18]. Through topological optimization, it becomes feasible to enhance a design concept by fulfilling the initial requirements effectively.

The solid isotropic material with penalization (SIMP) method is utilized to optimize a compliant mechanism. This approach forecasts material distribution within the designated design space, considering the type of applied load, as described by [19].

SIMP Approach

In the SIMP method, each finite element is assigned a variable known as the pseudo density, which can range from zero (indicating the absence of the material) to one (indicating the presence of the material). Conversely, the homogenization method generates topologies similar to those obtained through SIMP. However, their utilization is more intricate due to the necessity of considering a more significant number of design variables and a longer processing time, as noted by [20]. The design area is divided into square finite elements, and optimization of the model is achieved through a material density-based approach, as described by [21].

$$E_e(x_e) = E_{min} + x_e^p(E_0 - E_{min}) \quad (1)$$

where $E_e(x_e)$ is the effective elastic modulus of the element, which depends on the material density x_e, E_0 is the elastic modulus of the solid material, and E_{min} is the minimum allowable elastic modulus, which is often chosen as a very small value to represent "void" material. Finally, p is the penalization parameter, which controls the interpolation between the elastic modulus of the solid material and the minimum elastic modulus. All terms are scalars.

The mathematical expression for the optimization is:

$$c(x) = U^T K U = \sum_{e=1}^{N} (x_e)^p u_e^T k_e u_e \quad (2)$$

$$\text{Subject to : } \frac{V(x)}{V_0} = f\text{: } KU = F\text{: } 0 < x_{min} \leq x \leq 1$$

where $c(x)$ is the compliance of the structure, which is a scalar value representing its overall stiffness; U is a global displacement vector of the entire structure; K is the global stiffness matrix of the structure; F is a vector representing the external force vector applied to the structure; N is the number of elements; e is the density variable for each element e, representing the material distribution; u_e^T is the transpose of the displacement vector u_e, similar to U^T; p is the penalty factor, controlling the interpolation between the solid and void material; k_e is the element stiffness matrix; $V(x)$ is a scalar representing the volume of the structure, which depends on the material distribution x; V_0 is a scalar value that represents the initial volume or reference volume of the structure; f is a scalar value that represents a ratio between the volume $V(x)$ and the initial volume V_0, representing a variable associated with the material density or distribution within the structure; and finally; x_{min} is a scalar value representing the minimum allowable material density.

The optimization problem was solved by implementing the software MATLAB® (version R2019a, developed by MathWorks, a company based in Natick, MA, USA) to develop a programming code based on various examples referenced in [22].

2.3. Experimental Characterization of Joint Forces in the Sternum

Before embarking on a detailed design of the compliant mechanism, it was imperative to ascertain the forces exerted on the costosternal joints. This knowledge serves as a foundational step, providing essential input for the subsequent development of the compliant mechanism.

The analysis aimed to determine the magnitude of forces in the costovertebral and costosternal joints under two distinct scenarios: typical and deep breathing, with consideration given to the bucket-handle movement and pump-handle movement.

2.3.1. Experiment Setup

The experimental setup comprised six Optitrack® cameras operating at 120 frames per second, with an image resolution of 1.3 megapixels each. This product was developed by Natural Point, a company based in Corvallis, OR, USA. The cameras were positioned atop a metal structure within the laboratory. Light reflectors affixed to a specialized suit using Velcro at specific points were utilized to capture linear displacements of the thorax, and they were utilized to measure displacements along the x, y, and z-axes. A total of 24 light reflectors were positioned on the head, shoulders, back, hands, and chest. Additionally, two more reflectors (A, B) were placed on the mid-thorax to measure the vertical sagittal and coronal displacements, as shown in Figure 5.

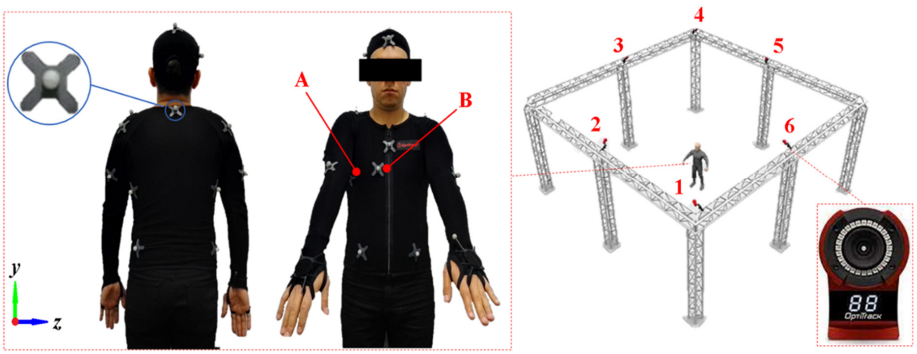

Figure 5. Experiment setup (A) light reflector positioned in coronal plane; (B) light reflector positioned in sagittal plane; (1–6) recording cameras.

Ten healthy young adult non-smoking male volunteers, with an average age of 26 years, participated in the study. Each participant wore a suit equipped with light reflectors. The calibration process yielded excellent results, with minimal error in the camera measurements, registering at 0.1 mm. First, the participants were instructed to position themselves in a standing position within the working volume of the cameras. They were asked to remain still and perform normal breathing for 15 s while their movements were recorded. Subsequently, the participants maintained the same position and were directed to take deep breaths up to their maximum lung capacity while their movements were recorded for an equal duration of 15 s. This procedure was repeated consistently for each participant.

2.3.2. Angular Displacements of the Ribs

The computed tomography (CT) scans of all ten participants were utilized. These scans included the necessary tissues required for virtual reconstruction, such as the sternum, vertebrae, and costal cartilage. Additionally, the first to the tenth ribs were considered for analysis, as the movement between these ribs is similar. This is particularly relevant as the seventh rib is attached to the last three ribs via the costovertebral cartilage, leading to uniformity in movement, as noted by [23]. The model reconstruction was carried out using SCAN IP® software (version 3.1, developed by Simpleware, a company based in Bradninch Hall, Exeter, UK), which generated a point cloud in STL format. This STL file could then be exported to FUSION 360® software (student version, developed by Autodesk, a company based in Mill Valley, CA, USA), where a solid model of each element could be obtained separately. With the separate models of each part, a comprehensive model of the thorax was constructed using SolidWorks® software (version 2016, developed by Dassault Systemes, a company based in Velizy-Villacoublay, France). This software facilitated the integration of the individual components into a unified representation of the thoracic structure.

Once the three-dimensional model of the thorax was developed, the geometry of each individual rib from the first to the seventh pair was determined. With knowledge of the rib geometry and the thorax's vertical displacements in the sagittal and coronal planes, it became possible to calculate the angular displacement of each rib using trigonometric functions. This approach allowed for a detailed analysis of the rib movements relative to the thoracic structure. The obtained angular displacements are illustrated in Figure 6, providing a visual representation of the rib movements relative to the thoracic structure. This figure serves as a valuable tool for understanding the dynamics of rib motion during breathing.

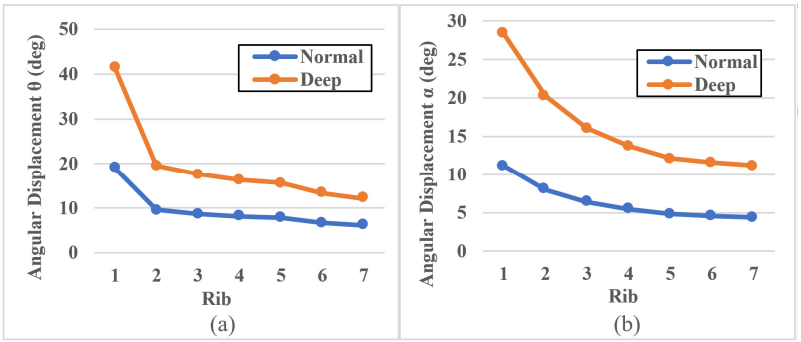

Figure 6. Calculated angular displacements of ribs 1–7 during normal and deep breathing: (**a**) bucket-handle angle θ; (**b**) pump-handle angle α.

2.3.3. Forces at Costosternal Joints

To determine the forces acting on the costosternal connections, MSC ADAMS® software (version 2023, developed by Hexagon, company based in Stockholm, Sweden), was employed. This software facilitates dynamic analysis and allows for the simulation of mechanical systems, making it suitable for assessing the forces exerted on the thoracic structure during breathing movements.

Once the model was loaded into MSC ADAMS® software, the bone density was set to 2000 kg/m^3, as indicated in the studies by [24,25]. This density value remained relatively constant due to the compact structure of bones, as mentioned by [26]. Additionally, the density of the costal cartilage is referenced from [27] for accurate material property assignment within the simulation. In MSC ADAMS® software, a fixed joint was defined between each rib and its corresponding costosternal cartilage. Additionally, spherical joints were established at the costovertebral and costosternal connections. Movement constraints were imposed on these joints to simulate physiological restrictions. For the costosternal joints, rotations along the x- and y-axes were restricted, allowing movement solely along the y-axis. The execution times and angular displacements were controlled using the step function to synchronize movements accurately. In contrast, the costovertebral joints had rotations restricted solely to the z-axis to emulate physiological movement patterns accurately, as indicated in Figure 7.

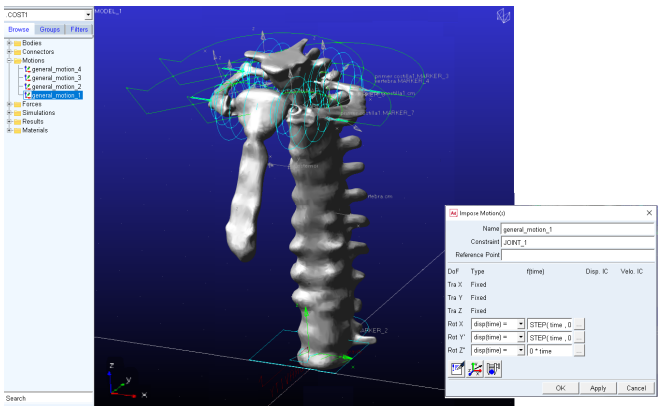

Figure 7. Vertebra–sternum–rib joint configuration in MSC ADAMS®.

These constraints ensured that the simulation replicated realistic biomechanical behavior. In MSC ADAMS® software, rotations along the y-axis were controlled using the step function to simulate the bucket-handle movement, while rotations along the x-axis were similarly controlled to represent the pump-handle movement.

2.4. Detailed Design

Since the generated topology exhibited discontinuous contours, post-processing was required to smooth the edges of the resulting geometries.

The first step involved interpreting the conceptual design derived from the of topology optimization method (TOM). This interpretation entailed deciding which pseudo-density values would be retained, determining which elements would constitute the final structure, and identifying those that would be disregarded. The three-dimensional model of the compliant mechanism was developed within SolidWorks®, ensuring the accuracy and smoothness of the final model. Three potential configurations of the compliant mechanism were evaluated, each featuring different rectangular cross-sectional dimensions: 0.7 × 2.9 mm, 0.6 × 2.5 mm, and 0.5 × 2.9 mm, as shown in Figure 8.

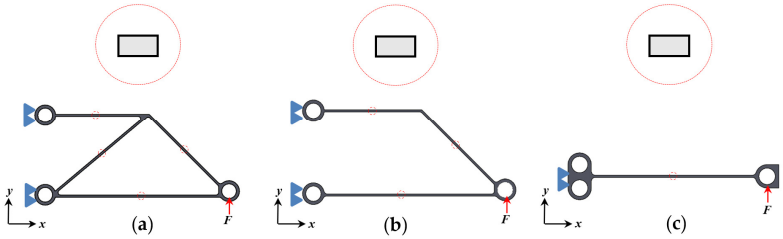

Figure 8. Three possible compliant mechanism configurations with rectangular cross-sections. (**a**) Configuration 1; (**b**) Configuration 2; (**c**) Configuration 3.

These configurations were assessed to determine which one produced the highest displacements, facilitating the selection of the most effective design.

The analysis of the results reveals that Configuration 3 in Table 1 exhibited more pronounced vertical displacements. Given that the primary aim of this study was to advance the development of a sternum endoprosthesis to improve ventilatory dynamics, Configuration 3 was selected as the compliant mechanism for the comprehensive design of the sternum endoprosthesis.

Table 1. Comparison of three different configurations for a compliant mechanism design.

			Cross-Section 0.7 × 2.9 mm		**Cross-Section 0.6 × 2.9 mm**		**Cross-Section 0.5 × 2.9 mm**	
Configuration	**Breathing Type**	**Force (N)**	**Vertical (mm)**	**Angular (deg)**	**Vertical (mm)**	**Angular (deg)**	**Vertical (mm)**	**Angular (deg)**
1	Deep	3.9	7.6×10^{-3}	0	1.3×10^{-2}	0.02	7.6×10^{-5}	0
	Normal	2.5	2.1×10^{-4}	0	8.1×10^{-3}	0.01	5×10^{-6}	0
2	Deep	3.9	5×10^{-1}	0.95	1.35	2.58	2.01	3.84
	Normal	2.5	7×10^{-2}	0.13	0.87	1.66	1.2	2.29
3	Deep	3.9	3.53	7.74	5.6	10.76	9.68	18.82
	Normal	2.5	2.26	4.97	3.59	6.87	6.2	11.93

2.5. Design Solution

Achieving a functional design entails the development of a design that effectively accomplishes its intended purpose or function. This process involves creating a mechanical system, component, or device that operates as intended, fulfilling the specified requirements and objectives. Essentially, attaining a functional design consists of crafting a product or system that performs its designated task effectively and efficiently while satisfying all pertinent criteria and requirements.

2.5.1. Static Simulation

After establishing the dimensional parameters and selecting the material for the sternum endoprosthesis, its three-dimensional design was developed using SolidWorks® software. Subsequently, the virtual model was imported into ANSYS Workbench® software (version 16.0, developed by Swanson Analysis Systems, company based in Canonsburg, PA, USA) to conduct numerical analysis employing the finite element method (FEM).

Boundary Conditions

The model's parametrization involved simulating the vertical load conditions exerted by each rib on the costosternal joints during human breathing. The most critical load condition for each rib, occurring during deep breathing, was considered. Vertical forces exerted during deep breathing were determined based on prior experimental analyses. Each force was applied along the positive *y*-axis at the first fixing hole of the compliant mechanism. Embedment was accounted for in the holes of the sternum closure and fixation plate, thereby limiting displacements and rotations. The material considered for the model was 6Al4V titanium, chosen for its excellent biocompatibility with the human body [28]. An isotropic model was utilized, employing a Young's modulus of 120 GPa and a Poisson's ratio of 0.3, as typically observed in titanium 6Al4V [29]. To facilitate finite element method (FEM) analysis, a quadratic formulation was adopted, resulting in high-order elements with an increased number of nodes (20 for hexahedrons and 10 for tetrahedra). This quadratic formulation improves result accuracy by offering a quadratic approximation. A bonded contact between the elements of the endoprosthesis was defined to prevent movement between them. This approach enabled us to concentrate on evaluating the structural integrity and load-bearing capacity of the endoprosthesis under specified loading conditions.

Mesh Sensitivity

A sensitivity analysis was crucial for determining the optimal size for each element in the mesh to achieve accurate results without excessively long processing times. Three numerical models were examined, each employing three different element sizes (0.5 mm, 0.25 mm, and 0.05 mm), all utilizing a quadratic formulation. Table 2 presents the parameters acquired for each element size.

Table 2. Comparison of the FEM analysis results for three different element sizes.

Element Size (mm)	Number of Elements	Number of Nodes	Solving Time (min)	Displacement on *y*-Axis (mm)	Von Mises Stress Max (MPa)
0.5	95,637	146,852	11	14.7	641.2
0.25	133,277	548,236	20	15.5	673.7
0.05	5,489,654	24,703,443	43	15.4	673.0

The values in Table 2 indicate that there was minimal variation between the mesh sizes of 0.05 mm and 0.25 mm. However, the processing time significantly increased when employing a mesh size of 0.05 mm. Consequently, an element size of 0.25 mm is appropriate.

Mesh Quality

Mesh quality analysis involves assessing the skewness and orthogonal parameters in the mesh elements. The skewness parameter quantifies the extent of deviation of an element's faces from an ideal shape, where all sides of the element possess identical dimensions. A skewness value of 0 indicates excellent geometric alignment of the component, while a value of 1 suggests severe deformation in its shape. Figure 9 illustrates the skewness for a mesh element size of 0.25 mm.

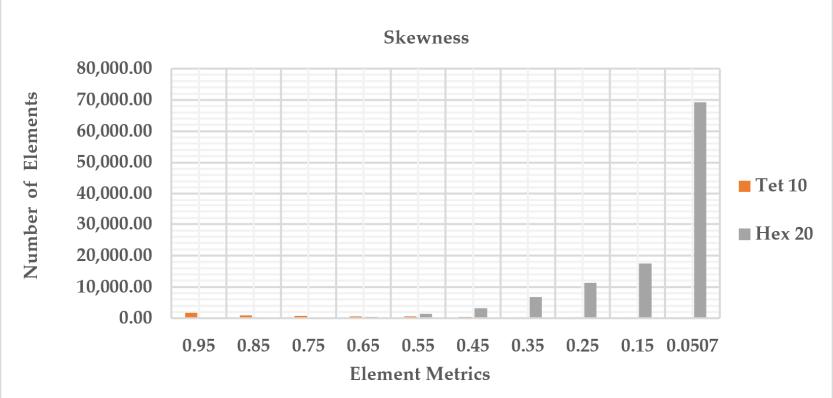

Figure 9. Skewness for a 0.25 mm element size.

The orthogonality parameter evaluates the disparity between the normal vectors on the faces of an element and those of its neighboring elements. An orthogonality value ranging from 0.95 to 1 is considered excellent, while a value from 0 to 0.001 is deemed unacceptable [30]. Figure 10 illustrates the orthogonality values for a mesh element size of 0.25 mm.

In the skewness plot, it is evident that the majority of the generated elements were hexahedrons with a skewness value of 0.05. Similarly, in the orthogonality plot, most elements were hexahedrons with an orthogonality value of 0.95. These metrics affirm that the mesh quality is satisfactory.

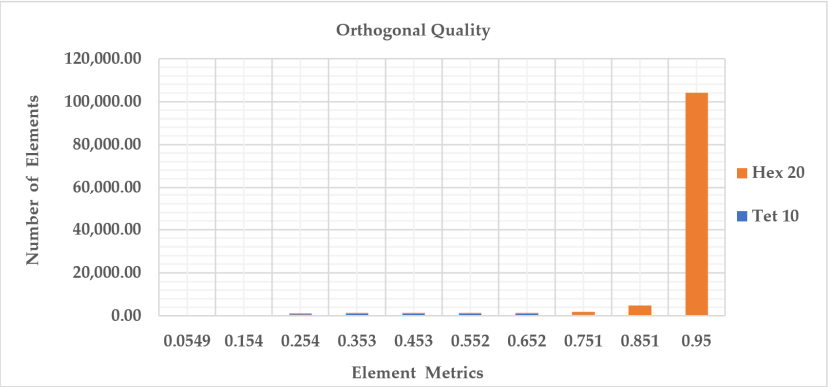

Figure 10. Orthogonality for a 0.25 mm mesh size.

2.5.2. Dynamic Simulation

A dynamic assessment of the sternal endoprosthesis was conducted to analyze its behavior concerning the accelerations and velocities it generates during its operation. MSC Adams® software was employed for this analysis. Given that the compliant mechanism generates movement without any articulation joint, a pseudo-rigid body model was utilized for the dynamic simulation.

Pseudo-Rigid Body Model (PRBM)

Modeling the compliant mechanism as a rigid body involved replacing each flexural joint with a torsion spring and a rotary joint, as proposed by [31]. For the mathematical analysis, the compliant mechanism selected from Table 1 was considered.

This element can be represented as a cantilever beam with a vertical force applied at the free end. A schematic configuration of the pseudo-rigid body model, depicting a cantilever beam with an applied vertical force at the free end, is illustrated in Figure 11.

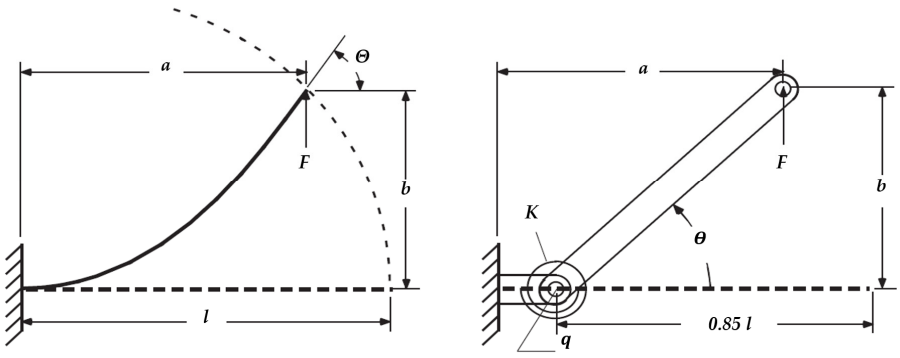

Figure 11. Pseudo-rigid body model for a cantilever beam with a vertical load at the free end.

To assess the suitability of a material for use in a compliant mechanism, it is important to consider the ratio between its flexion yield stress and its Young's modulus, as suggested by [32]. The mechanical performance parameters of the compliant mechanism can be determined using the following equations.

$$R = \left(\frac{S_y}{E}\right) \times 1000 \tag{3}$$

$$K = 2.258\left(\frac{EI}{l}\right) \tag{4}$$

$$F = \frac{K\theta}{\gamma l \cos\theta} \tag{5}$$

$$\sigma_{max} = \frac{Fac}{I} \tag{6}$$

$$a = l[1 - \gamma(1 - \cos\theta)] \tag{7}$$

where k is the torsion spring stiffness, E is the material's Young's modulus, I is the moment of inertia, l is the length of the beam, F is the applied force, θ is the link angle expressed in radians, γ is the characteristic radius factor with a value of 0.85 for this configuration [33], σ_{max} is the maximum stress, a is the horizontal deflection of the link, and c is the distance from the neutral axis to the surface of the beam.

The quantitative values were derived through the analytical development of the mechanical performance parameters for the compliant mechanism. Table 3 provides a summary of all these parameters.

Table 3. Mechanical performance parameters of the compliant mechanism.

Parameter	Value
Torsion spring stiffness, K	0.471 Nm
Required force, F	3.79 N
Maximum stress, σ_{max}	672 MPa
Horizontal deflection, a	29.55 mm

Virtual Kinematic Simulation

MSC ADAMS® software was utilized to simulate the pseudo-rigid body model for a kinematic characterization, as illustrated in Figure 12.

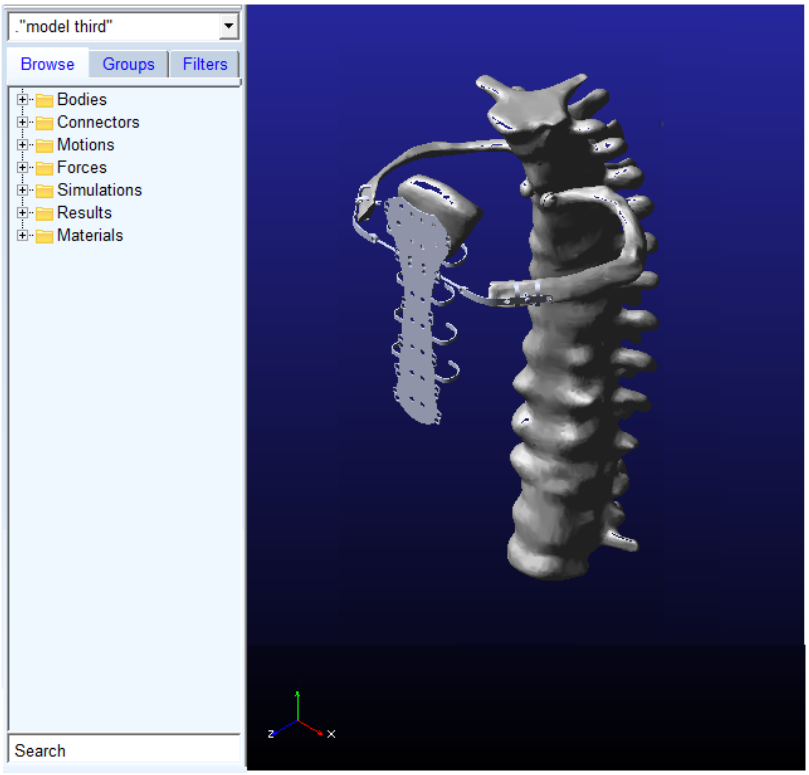

Figure 12. Compliant mechanism model simulated in MSC Adams ® software.

Displacements and rotations were constrained in the compliant mechanism fixation holes. Titanium 6Al4V was chosen as the material for all elements of the model, with its density set to 4430 kg/m^3. In the bending zone of the mechanism, a torsion spring stiffness was determined, and the calculated value (K = 0.471 Nm) was assigned. Kinematic analysis was performed by applying an angular displacement representing deep breathing to each

rib as input in the prosthesis arm. This angular displacement was applied over a duration of 2 s for lifting and an additional 2 s for descent, using a step function.

3. Results

This section presents the results obtained at each stage of the methodology depicted in Figure 1, showcasing the outcomes of the various stages.

3.1. Conceptual Design

The simulation yielded a two-dimensional model with regions colored in white and black, as illustrated in Figure 13. The white regions signify the absence of material, indicating the areas unaffected by the load. Conversely, the black regions denote areas where material may be present, representing zones where load transmission occurs. However, the resulting model does not consider the desired range of deflections. Hence, elements of the model can be eliminated to achieve more significant displacements under the same load.

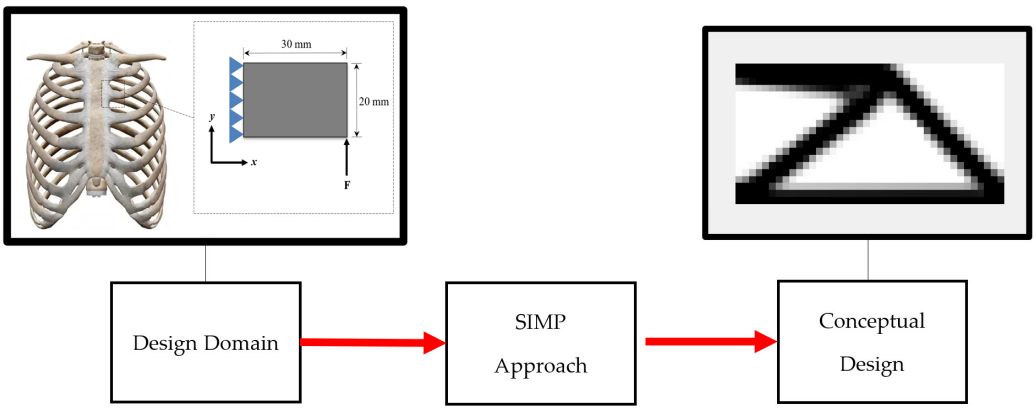

Figure 13. Conceptual design of a sternum endoprosthesis compliant mechanism.

3.2. Forces at Costosternal Joints

The maximum vertical forces in the costosternal joints for each pair of ribs during the inspiration–expiration respiratory cycle, were computed separately for normal breathing and deep breathing at the maximum lung capacity. The analysis covered the first pair to the seventh pair of ribs. The calculated results are presented in Table 4.

Table 4. Maximum vertical forces in costosternal joint reached during normal and deep breathing.

Costosternal Joint Rib Number	Normal Breathing Vertical Force (N)	Deep Breathing Vertical Force (N)
1	1	1.9
2	2.5	3.9
3	1.8	2.6
4	1.4	2.2
5	1.5	2.7
6	2	3.3
7	2	2.9

3.3. Detailed Design

When designing our sternum endoprosthesis, we specifically targeted ribs from the second to the sixth, excluding the first and seventh ribs. This choice was informed by the existing solutions outlined in the Section 1, which underscored the increased incidence of damage in these ribs. Moreover, given the seventh rib's attachment to the sixth via cartilage, any movement induced in the sixth rib would inevitably impact the seventh as well. Consequently, our design approach focuses on addressing the ribs most frequently affected

while also taking biomechanical considerations into account to ensure the effectiveness of our solution. Figure 14 depicts the sternum endoprosthesis model (1), comprising a closure and fixation plate to the sternum (2), a rear support plate (3), and a compliant mechanism with anchoring to the rib (4), with each element corresponding to the number of free ribs to be anchored to the endoprosthesis. All these components are interconnected using double-threaded screws (5). The entire endoprosthesis is manufactured from a titanium 6Al4V alloy, selected for its biocompatibility with the human body.

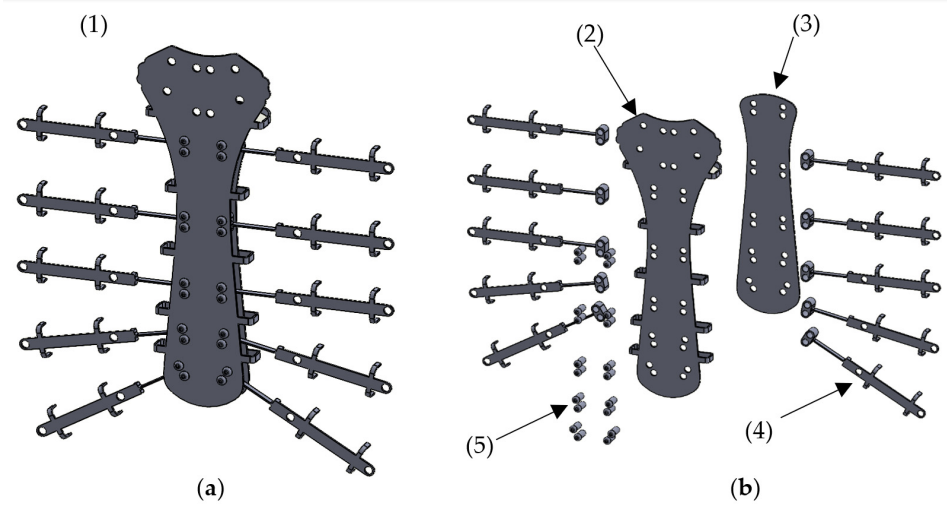

Figure 14. Tridimensional model of a sternum endoprosthesis. (**a**) sternum endoprosthesis full assembly; (**b**) expanded view; (1) sternum endoprosthesis; (2) sternum closure fixation plate; (3) rear support plate; (4) compliant mechanism; (5) fixation screws.

The compliant mechanism design consists of the selected Configuration 3 in Table 1, along with a flat extension of 0.79 mm thickness (6) to facilitate its fixation to the rib. It features two 3.5 mm holes (7) for attachment to the sternum closure fixation plate (2) and the rear support plate (3). Additionally, it includes two 3.5 mm holes for fixation to the rib (8) as the primary fixation method and two pairs of flexible hooks (9) as the secondary fixation method. The compliant mechanism has a deflection zone length of 30 mm, with the remaining length varying according to the length of the rib to be joined. The remaining length can be bent to conform to the curvature of the rib. The applied input force (10) is transmitted from the rib to the mechanism through the left 3.5 mm hole (8). This input force flexes the compliant mechanism (4), resulting in a linear vertical displacement that can be expressed as angular displacement. The three-dimensional model of the compliant mechanism with anchoring to the rib is depicted in Figure 15.

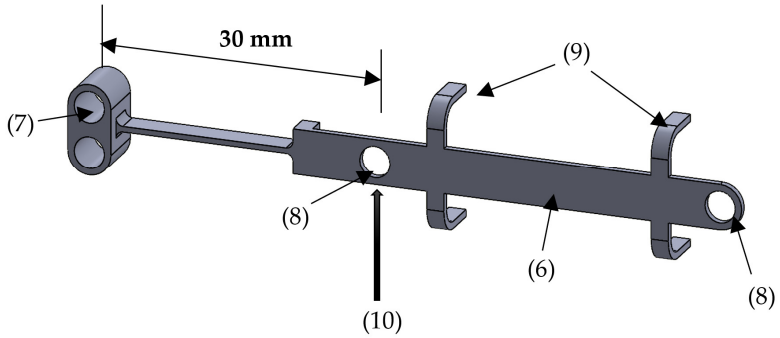

Figure 15. Compliant mechanism design. (6) rib fixation plate; (7) mechanism fixation holes; (8) rib fixation hole; (9) flexible hooks; (10) input force.

Sharp edges on prosthetic components can present significant risks to patients. When implanted, these sharp edges may cause tissue irritation, inflammation, or injury. It is necessary to avoid sharp edges by employing precision manufacturing techniques, such as machining, grinding, or deburring; thus, we can effectively remove sharp edges and create smooth surfaces on the prosthetic components. This process not only reduces the risk of tissue trauma but also enhances patient comfort and promotes better integration of the prosthesis with the surrounding tissues.

3.3.1. Static Simulation

The results obtained from the numerical analysis applied to the mechanism with the selected cross-section of 0.6 × 2.9 mm are presented. The simulation yielded displacement graphs along the *y*-axis. Figure 14 illustrates the displacements in the complete sternum endoprosthesis.

In Figure 16, it is evident that the most substantial vertical displacement of 15.49 mm occurred in the compliant mechanism for the first rib. This plot illustrates that the greatest displacement was generated in the free parts of the mechanisms, which connect with the ribs, and from there, the vertical displacement decreased linearly until reaching the fixed zone. Additionally, it can be observed that only the compliant mechanisms of each rib underwent displacements, while the fixation and closure plate to the sternum remained unaffected by the applied forces. The primary common characteristic among them is their linear behavior. As expected, the compliant mechanism of the second rib exhibited the most significant displacement, reaching 15.49 mm. The compliant mechanisms of ribs 3, 4, 5, and 6 display similar displacement patterns.

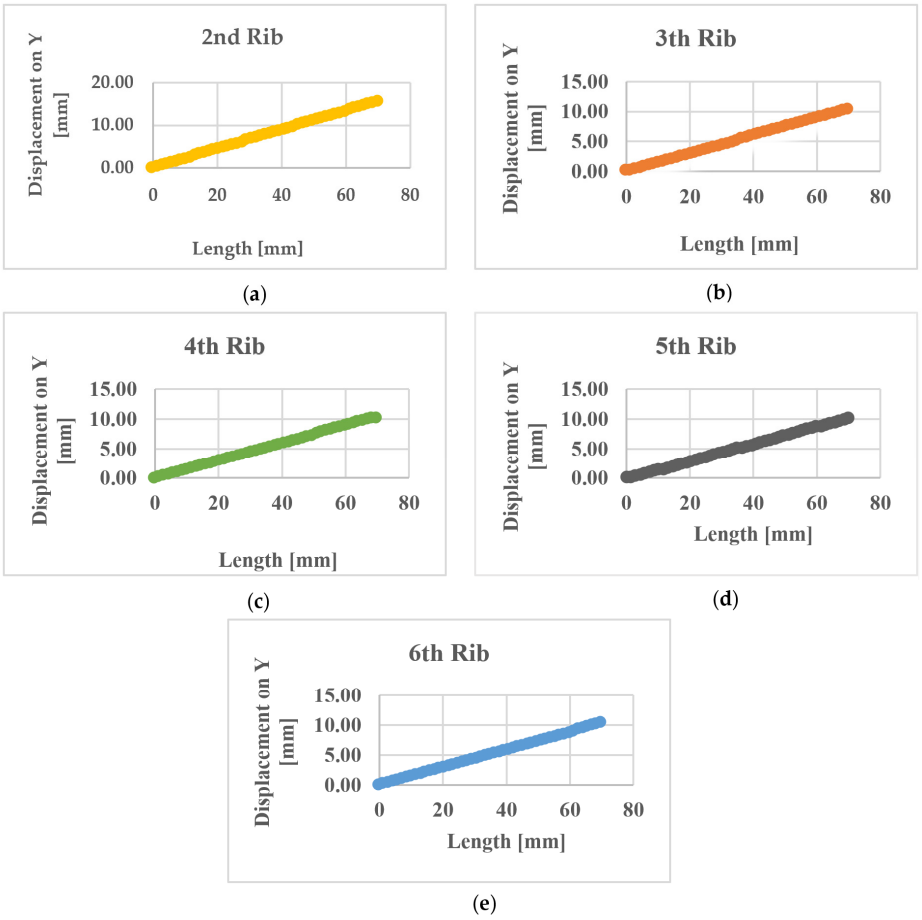

Figure 16. Plot results of directional displacements on the *y*-axis: (**a**) second rib; (**b**) third rib; (**c**) fourth rib; (**d**) fifth rib; (**e**) sixth rib.

Another crucial result to consider is the maximum stress value induced in the complete sternum endoprosthesis due to the applied load. The maximum stress concentration was determined from a plot of the model, illustrated in Figure 17.

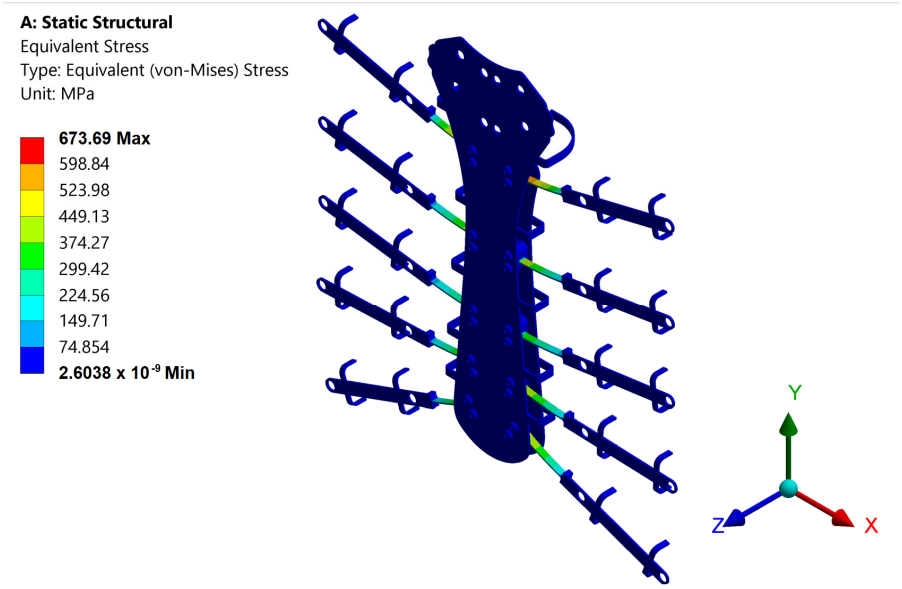

Figure 17. Plot of von-Mies stress concentration.

In Figure 17, the material remains within its elastic zone, as the maximum stress generated in the material is 673.6 MPa, while the yield stress of titanium 6Al4V is 924 MPa. This observation confirms that the mechanism does not experience permanent deformations.

As a summary of the results derived from finite element method (FEM) analysis, Table 5 presents the maximum stress concentrations and vertical displacements obtained in each compliant mechanism during deep breathing.

Table 5. Obtained results from FEM analysis during deep breathing.

Compliant Mechanism Rib Number	Applied Force (N)	Vertical Displacement (mm)	Angular Displacements (deg)	Stress Concentration (MPa)
2nd	3.9	15.5	12.3	673.6
3rd	2.6	10.3	8.2	456.7
4th	2.2	10.2	8	390.2
5th	2.7	10.1	8	419.9
6th	3.3	10.2	8	461.5

3.3.2. Kinematic Simulation

An analysis was conducted to obtain the velocity and acceleration graphs of the compliant mechanisms corresponding to ribs 2, 3, 4, 5, and 6. Figure 18 displays the velocity curves. On the *y*-axis, there is a positive peak, indicating a maximum speed reached before decreasing to zero. This suggests that the velocity along the *z*-axis experienced rapid acceleration followed by deceleration, returning to zero. The velocity along the *z*-axis exhibited a complete oscillation, initiating and concluding at zero, with a negative peak and a positive valley. This indicates that the velocity along the *y*-axis transitioned from negative to positive before returning to zero. Conversely, the velocity along the *x*-axis remained relatively stable near zero, with a slight negative deviation. This suggests that the velocity along the *x*-axis remained nearly constant and close to zero throughout the analyzed period.

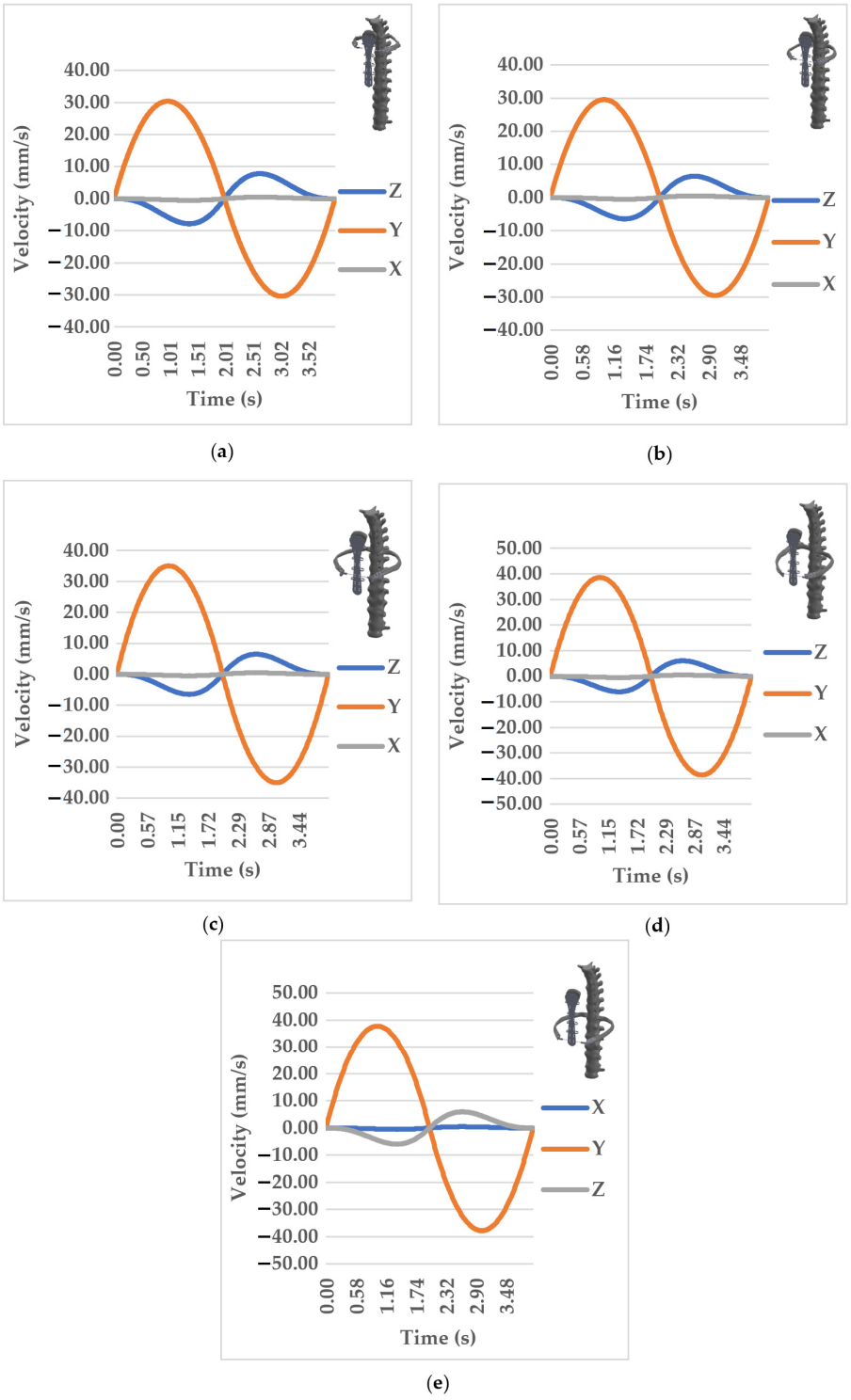

Figure 18. Plot results for velocity in compliant mechanisms: (**a**) second pair; (**b**) third pair; (**c**) fourth pair; (**d**) fifth pair; (**e**) sixth pair.

In Figure 19, the acceleration curves indicate distinct behaviors along each axis. Along the *x*-axis, the acceleration curve remains constant at a value close to 0 mm/s^2, suggesting minimal variation in acceleration along that direction. The curve on the *y*-axis exhibits positive acceleration, reaching its maximum peak before decreasing to a negative acceleration. This pattern signifies a rapid change in the acceleration's direction along the *y*-axis.

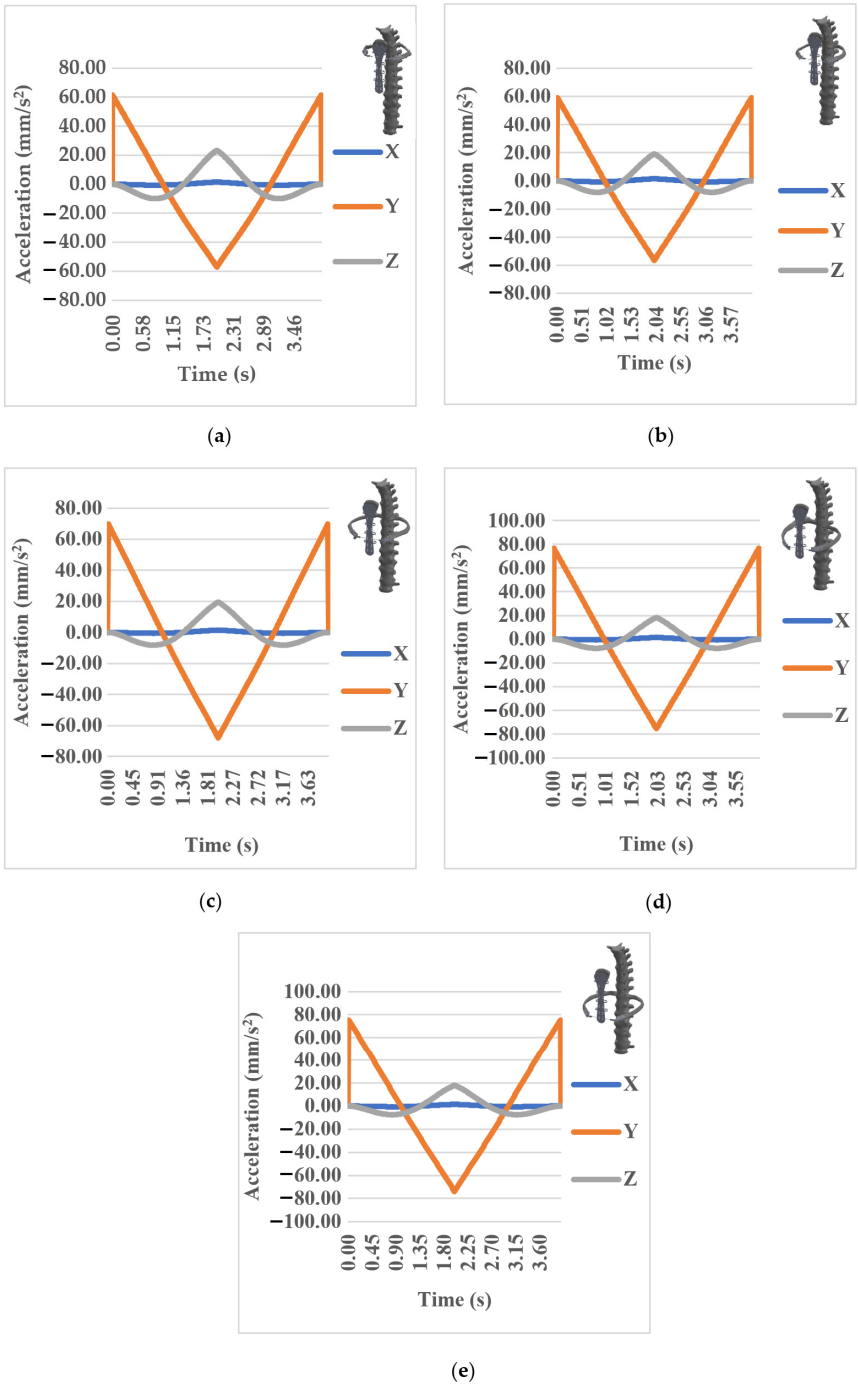

Figure 19. Plot results for acceleration in compliant mechanisms: (**a**) second pair; (**b**) third pair; (**c**) fourth pair; (**d**) fifth pair; (**e**) sixth pair.

Similarly, the curve on the *z*-axis shows a behavior analogous to the *y*-axis curve but with lower values. It reaches its maximum acceleration before transitioning to the minimum value, indicating a rapid change in the acceleration's direction along the *z*-axis.

4. Discussion

This study aimed to develop an innovative sternum prosthesis with the objective of enhancing respiratory dynamics following sternum resection procedures resulting from various pathologies.

The movements of various pairs of ribs were analyzed in terms of pump- and bucket-handle movements. The obtained results exhibit a striking resemblance to those reported

in [34] for normal breathing, as depicted in Figure 20. Specifically, there was minimal variation observed in the bucket-handle angle θ.

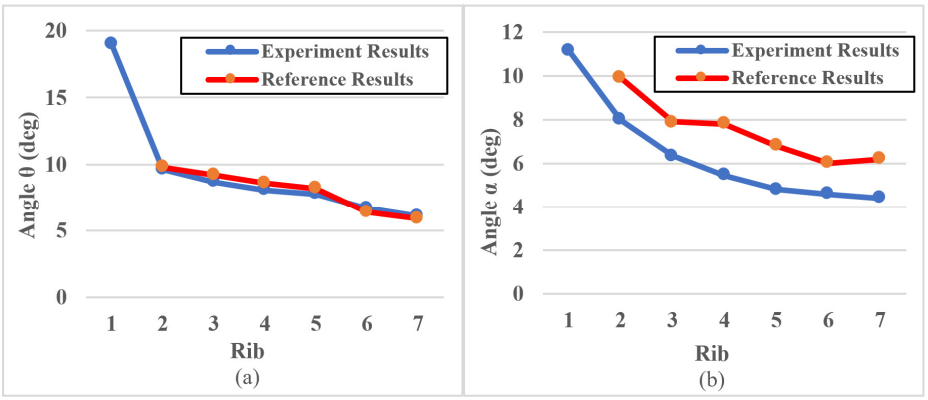

Figure 20. Results for bucket-handle angle (θ) and pump-handle angle (α) of ribs 1–7: (**a**) comparison of bucket-handle angle (θ) between experimental results from this work and reference results [34] during normal inspiration; (**b**) comparison of pump-handle angle (α) between experimental results from this work and reference results [34] during normal inspiration.

The developed sternum endoprosthesis is applicable for cases involving partial or total resection of the sternum, as illustrated in Figure 21. This necessity typically arises in the presence of a cancerous tumor. The affected region, along with a portion of adjacent ribs, is excised, the extent of which varies depending on the tumor's size. The sternum endoprosthesis serves to replace the removed sternal segment and facilitates the attachment of the free ribs, thereby restoring the structural integrity of the rib cage.

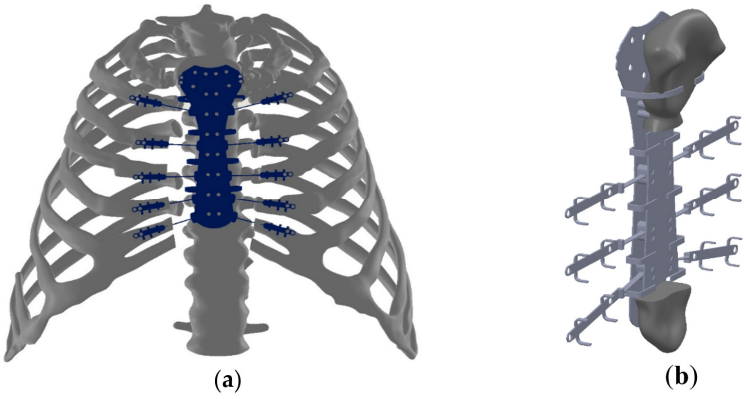

Figure 21. Sternum endoprosthesis application: (**a**) total resection of the sternum; (**b**) partial resection of the sternum.

Another application of the sternum prosthesis is for sternum closure. In this scenario, the plate is affixed to the outer surface of the divided sternum. The plate is designed to be thin enough to conform to the curves of the sternum. Initial fixation is accomplished using double-threaded screws, which secure the plate to the bone. Subsequently, secondary fixation is achieved using flexible hooks that encircle the sternum, thereby facilitating stabilization of the segments. Figure 22 depicts a representative schematic of sternum closure.

As a future direction for this research, it is imperative to fabricate a prototype and conduct experimental characterization of the sternum endoprosthesis under identical load conditions as proposed, aiming to validate the numerically obtained results. Furthermore, collaboration with surgeons experienced in this type of surgery is essential to facilitate its clinical implementation.

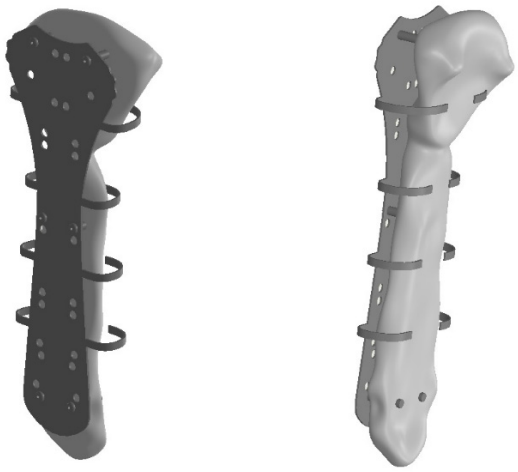

Figure 22. Sternum closure and fixation plate implemented in sternum closure operation.

5. Conclusions

A novel proposal for a human sternum endoprosthesis has been developed to address the challenge of enhancing ventilatory mechanics within the human thorax when utilizing such an endoprosthesis.

The characterization of the vertical forces acting on the costosternal junctions was conducted using the OPTITRACK® experimental photogrammetry equipment available at IPN SEPI ESIME Zacatenco. Through this experimental test, it was established that the vertical displacements occurring in various thoracic regions were highly consistent, with a marginal 3% variation observed between the upper and lower portions of the rib cage. The primary factor influencing angular displacements of individual ribs was their geometry. Consequently, the smaller size of the first ribs resulted in greater angular displacements.

The integration of a compliant mechanism enabled the generation of maximum angular displacements up to 10.76 degrees. However, the experimental test revealed that the highest displacement occurred at the second rib, reaching 19.3 degrees, representing a 56% improvement in movement recovery. The maximum angular displacement resulted in a stress concentration of 672 MPa within the compliant mechanism, which falls below the yield stress of titanium 6Al4V, measured at 924 MPa. Despite the slight variation in stress levels, it was ensured that the material operated within its elastic range. Moreover, this stress occurred under the most demanding loading condition, deep breathing. Under the more common load condition of normal breathing, the compliant mechanism experienced a stress of 431 MPa, even lower than the material's yield stress, yielding a safety factor of 2.1 for normal breathing and 1.3 for deep breathing. The novelty of the design of the sternum fixation and closure plate lies in its versatility. It serves the dual purpose of replacing a segment of the sternum while also providing a platform for attaching compliant mechanisms that connect to each rib through its strategically placed holes. Additionally, this plate can be employed independently for sternum closure in open-heart surgeries.

Since all elements are constructed from a 6Al4V titanium sheet, measuring 0.7 and 0.5 mm in thickness, a lightweight design with a calculated mass of 37 g was achieved.

The utilization of the pseudo-rigid body model effectively validated the numerically obtained results. Employing this model yielded a negligible variation of 0.1% for the maximum stress generated within the flexible mechanism.

6. Patents

As a result of this research, a patent for the design of the sternum prosthesis was secured. Registrations were obtained in Mexico City (MX/U/2021/000651) and Italy (No. 102020000013486, 08-06-2020).

Author Contributions: Conceptualization, C.R.T.-S. and O.R.; methodology, C.R.T.-S. and O.R.; software, O.R.; validation, C.R.T.-S. and M.C.; formal analysis M.C.; investigation, M.C. resources, C.R.T.-S.; data curation, O.R.; writing—original draft preparation, O.R. and C.R.T.-S.; writing—review and editing M.C.; visualization M.C.; supervision, C.R.T.-S.; project administration, C.R.T.-S.; funding acquisition, C.R.T.-S. All authors have read and agreed to the published version of the manuscript.

Funding: The authors are thankful to the Consejo Nacional de Humanidades Ciencias y Tecnologías (CONAHCyT), and the Instituto Politécnico Nacional for the support received from projects SIP 20240701 and SIP 20242785 as well as the EDI grant, all from SIP/IPN.

Institutional Review Board Statement: Not applicable.

Informed Consent Statement: Informed consent was obtained from all subjects involved in the study.

Data Availability Statement: Data is contained within the article.

Acknowledgments: The authors acknowledge the participation of the robotics group of LARM2 incorporated at Tor Vergata University in Rome, Italy.

Conflicts of Interest: The authors declare no conflicts of interest.

References

1. Remolina-Medina, C.E.; Arévalo-Zamora, C. Surgical resection of the sternum with reconstruction with titanium bars and biological mesh prosthesis. Case report. *Neumol. Y Cirugía De Tórax* **2017**, *76*, 30–35. [CrossRef] [PubMed]
2. Hever, P.; Singh, P.; Eiben, I.; Eiben, P.; Nikkhah, D. The management of deep sternal wound infection: Literature review and reconstructive algorithm. *JPRAS Open* **2021**, *28*, 77–89. [CrossRef] [PubMed]
3. Shah, A.A.; D'Amico, T.A. Primary chest wall tumors. *J. Am. Coll. Surg.* **2010**, *210*, 360–366. [CrossRef]
4. Klei, D.S.; de Jong, M.B.; Öner, F.C.; Leene, L.P.; Van Wessem, K.J. Current treatment and outcomes of traumatic sternal fractures—A systematic review. *Int. Orthop.* **2019**, *43*, 1455–1464. [CrossRef]
5. Sillar, W. The crushed chest. *J. Bone Jt. Surg.* **1961**, *16*, 738–745. [CrossRef]
6. Alonso, F.; De Linera, F.A. Resection of the entire sternum and replacement with acrylic resin Report of a case of giant chondromyxoid fibroma. *J. Thorac. Cardiovasc. Surg.* **1971**, *62*, 271–278. [CrossRef]
7. Aranda, J.; Jiménez, M.; Rodríguez, M.; Varela, G. Tridimensional titanium-printed custom-made prosthesis for sternocostal reconstruction. *Eur. J. Cardio-Thorac. Surg.* **2015**, *48*, e92–e94. [CrossRef] [PubMed]
8. Cano, J.R.; Hernández, F.; Pérez, D.; López, L. Reconstruction of The Anterior Chest Wall with A 3D-Printed Biodynamic Prosthesics. *J. Thorac. Cardiovasc. Surg.* **2017**, *155*, 59–60. [CrossRef]
9. Wang, B.; Guo, Y.; Tan, J.; Yu, F. Three-dimensional custom-made carbon-fiber prosthesis for sternal reconstruction after sarcoma resection. *Thorac. Cancer* **2019**, *10*, 1500–1502. [CrossRef]
10. Halverson, P.A.; Bowden, A.E.; Howell, L.L. A Pseudo-Rigid-Body Model of the Human Spine to Predict Implant-Induced Changes on Motion. *ASME J. Mech. Rob.* **2011**, *3*, 041008. [CrossRef]
11. Dodgen, E.; Stratton, E.; Bowden, A.; Howell, L. Spinal Implant Development, Modeling, and Testing to Achieve Customizable and Nonlinear Stiffness. *J. Med. Devices-Trans. ASME* **2012**, *6*, 021010. [CrossRef]
12. Hong, S.W.; Yoon, J.; Kim, Y.J.; Gong, H.S. Novel Implant Design of the Proximal Interphalangeal Joint Using an Optimized Rolling Contact Joint Mechanism. *J. Orthop. Surg. Res.* **2019**, *14*, 212. [CrossRef]
13. Smelt, J.; Pontiki, A.; Jahangiri, M.; Rhode, K.; Nair, A.; Bille, A. Three-dimensional printing for chest wall reconstruction in thoracic surgery: Building on experience. *Thorac. Cardiovasc. Surg.* **2020**, *68*, 352–356. [CrossRef] [PubMed]
14. Pahl, G.; Beitz, W.; Feldhusen, J.; Grote, K.-H. *Engineering Design: A Systematic Approach*; Springer: London, UK, 2007; pp. 159–210.
15. Aquilini, M.; Ceccarelli, M. Design and Testing of RESPIRholter Device for Respiratory Monitoring. In *Advances in Italian Mechanism Science*; Niola, V., Gasparetto, A., Quaglia, G., Carbone, G., Eds.; IFToMM Mechanisms and Machine Science: Napoli, Italy, 2022; Volume 122, pp. 480–487.
16. Guzmán-López, S.; Elizondo-Omaña, R. *Human Anatomy in Clinical Cases: Learning Centered on the Clinical Reasoning (Anatomía Humana en Casos Clínicos: Aprendizaje Centrado en el Razonamiento Clínico) (Spanish Edition)*; Editorial Medica Panamericana: Mexico City, Mexico, 2012; p. 41.
17. Rajani, P.; Ratnaprabha, P. Assessment of reference values of chest expansion among healthy adults in pune. *Int. J. Physiother. Res.* **2017**, *5*, 1819–1823.
18. De Leon, D.M.; Alexandersen, J.; Fonseca, J.S.; Sigmund, O. Stress-constrained topology optimization for compliant mechanism design. *Struct. Multidiscip. Optim.* **2015**, *52*, 929–943. [CrossRef]
19. Bruns, T.E. A reevaluation of the SIMP method with filtering and an alternative formulation for solid–void topology optimization. *Struct. Multidiscip. Optim.* **2005**, *30*, 428–436. [CrossRef]
20. Lee, E.; Gea, H.C. A strain based topology optimization method for compliant mechanism design. *Struct. Multidiscip. Optim.* **2014**, *49*, 199–207. [CrossRef]

21. Wang, M.Y.; Chen, S. Compliant mechanism optimization: Analysis and design with intrinsic characteristic stiffness. *Mech. Based Des. Struct. Mach.* **2009**, *37*, 183–200. [CrossRef]
22. Zhu, B.; Zhang, X.; Zhang, H.; Liang, J.; Zang, H.; Li, H.; Wang, R. Design of compliant mechanisms using continuum topology optimization: A review. *Mech. Mach. Theory* **2020**, *143*, 103622. [CrossRef]
23. Wilson, T.A.; Rehder, K.; Krayer, S.; Hoffman, E.A.; Whitney, C.G.; Rodarte, J.R. Geometry and respiratory displacement of human ribs. *J. Appl. Physiol.* **1987**, *62*, 1872–1877. [CrossRef]
24. Mughal, U.; Khawaja, H.; Moatamedi, M. Finite element analysis of human femur bone. *Int. J. Multiphysics* **2015**, *9*, 101–108. [CrossRef]
25. Li, Z.; Kindig, M.W.; Subit, D.; Kent, R.W. Influence of mesh density, cortical thickness and material properties on human rib fracture prediction. *Med. Eng. Phys.* **2010**, *32*, 998–1008. [CrossRef]
26. Caeiro, J.R.; Gonzalez, P.Y.; Guede, D. Biomechanics and bone (& II): Trials in different hierarchical levels of bone and alternative tools for the determination of bone strength. *Rev. De Osteoporos. Y Metab. Miner.* **2013**, *5*, 99–108.
27. Furusu, K.; Watanabe, I.; Kato, C.; Miki, K.; Hasegawa, J. Fundamental study of side impact analysis using the finite element model of the human thorax. *JSAE Rev.* **2001**, *22*, 195–199. [CrossRef]
28. Oldani, C.; Dominguez, A. Titanium as a Biomaterial for Implants. *Recent Adv. Arthroplast.* **2012**, *218*, 149–162.
29. Fiaz, H.S.; Settle, C.R.; Hoshino, K. Metal additive manufacturing for microelectromechanical systems: Titanium alloy (Ti-6Al-4V)-based nanopositioning flexure fabricated by electron beam melting. *Sens. Actuators A Phys.* **2016**, *249*, 284–293. [CrossRef]
30. Gok, K.; Inal, S.; Gok, A.; Gulbandilar, E. Comparison of effects of different screw materials in the triangle fixation of femoral neck fractures. *J. Mater. Sci. Mater. Med.* **2017**, *28*, 81. [CrossRef] [PubMed]
31. Howell, L.L.; Midha, A.; Norton, T.W. Evaluation of equivalent spring stiffness for use in a pseudo-rigid-body model of large-deflection compliant mechanisms. *ASME J. Mech. Des.* **1996**, *118*, 126–131. [CrossRef]
32. Mattson, C.A.; Howell, L.L.; Magleby, S.P. Development of commercially viable compliant mechanisms using the pseudo-rigid body model: Case studies of parallel mechanisms. *J. Intell. Mater. Syst. Struct.* **2004**, *15*, 195–202. [CrossRef]
33. Murphy, M.D.; Midha, A.; Howell, L.L. The topological synthesis of compliant mechanisms. *Mech. Mach. Theory* **1996**, *31*, 185–199. [CrossRef]
34. Zhang, G.; Chen, X.; Ohgi, J.; Miura, T.; Nakamoto, A.; Matsumura, C.; Sugiura, S.; Hisada, T. Biomechanical simulation of thorax deformation using finite element approach. *Biomed. Eng. Online* **2016**, *15*, 15–18. [CrossRef] [PubMed]